Quantifying the early stages of plasticity through nanoscale experiments and simulations

Krystyn J. Van Vliet,[1,*] Ju Li,[2,†] Ting Zhu,[2] Sidney Yip,[1,2] and Subra Suresh[1,‡]
[1]*Department of Materials Science and Engineering, Massachusetts Institute of Technology, Cambridge, Massachusetts 02139*
[2]*Department of Nuclear Engineering, Massachusetts Institute of Technology, Cambridge, Massachusetts 02139*
(Received 14 June 2002; published 25 March 2003)

Nucleation and kinetics of defects at the atomic scale provide the most fundamental information about the mechanical response of materials and surfaces. Recent advances in experimental and computational analyses allow us to study this phenomenon in the context of nanoindentation and localized mechanical probing of surfaces. Here, we present an analytical formulation of the elastic limit that predicts the location and slip character of a homogeneously nucleated defect in crystalline metals, and extend this formulation to the atomic scale in the form of an energy-based, local elastic stability criterion, termed the Λ criterion. We demonstrate that this approach can be incorporated efficiently into computational methods such as molecular dynamics and finite-element models. Furthermore, we validate and calibrate the Λ criterion directly through nanoindentation experiments and two-dimensional experimental analogs such as the bubble raft model. We outline explicitly a compact and efficient application of the Λ criterion within the context of a nonlinear, interatomic potential finite-element model (IPFEM). Further, we report three-dimensional molecular dynamics simulations in several face-centered cubic systems that elucidate the transition from the initiation to the early stages of plasticity during nanoindentation of metals, as characterized by homogeneous and heterogeneous nucleation of up to hundreds of dislocations. Correlation of these simulations with direct observations from nanoindentation experiments provides atomistic insights into the early stages of plasticity.

DOI: 10.1103/PhysRevB.67.104105 PACS number(s): 62.25.+g, 02.70.−c, 81.07.−b, 81.40.−z

I. INTRODUCTION

A fundamental transition in the mechanical behavior of materials is the shift from elastic (reversible) to plastic (irreversible) deformation. In crystalline metals at room temperature, this process is mediated predominantly by the nucleation and motion of dislocations. Theoretical frameworks have been established for dislocation nucleation at the atomic scale,[1–4] but currently no such framework exists for the so-called homogeneous nucleation mechanism, where defects are nucleated in the crystal in the absence of other nearby, preexisting defects. Indeed, although we have analytical formulations of the self-energy of a single dislocation, the conditions necessary to *nucleate* dislocations in the bulk and in thin films are unresolved.[5] Currently we rely on continuum concepts such as critical resolved shear stress and yield strength to quantify the onset of plasticity in metals, even though this transition is initiated at the atomic scale.

The need for nanoscale interpretation of defect nucleation is even more pressing now that a sophisticated range of experimental and computational tools are available to explore material response near the atomic level. In fact, recent developments in both multiscale computational modeling and nanoscale experiments allow these two distinct methods of material analysis to explore mechanical behavior at length scales comparable to one another. Nanoscale experiments via nanoindentation, atomic force microscopy, and other techniques can probe mechanically the elastic stability of crystals at subnanometer displacements and large local contact strains. Results from these and other related experiments have indicated that such contact can induce elastic instabilities that have been deposited as evidence of homogeneous dislocation nucleation. The chief obstacle to further validation of such experiments is the considerable difficulty in determining atomic scale activities in three dimensional (3D), opaque crystals, as well as the challenges associated with conducting sufficiently clean experiments at this length scale in initially defect-free materials.

Atomic scale simulations such as molecular dynamics (MD) can provide the required visualization and precise control over characterization of the evolving defect microstructure over a very well defined, though limited, time period. Indeed, several researchers have modeled indentation of 3D, fcc crystals and observed dislocation activity.[6–10] However, the length scales in such studies are limited by computational resources, resulting in indenter tip dimensions and strain rates that are incongruent with those attainable in experiments. Even when computational analyses incorporate multiple length scales to approach realistic dimensions, such as in the quasicontinuum method of Tadmor *et al.*,[11] the observations have not been sufficiently well calibrated against experiments and do not culminate in predictive capabilities. Thus, it appears that although both experiments and computational modeling have the potential to explore the same phenomenon, neither has been constructed in such a way that its results truly address the hypotheses and quantitative capabilities of the other.

In this work, we outline experimental, analytical, and computational analyses of nanoindentation that were designed together to elucidate the mechanisms by which localized contact can induce the transition from elastic to plastic deformation in an initially defect-free crystal, and the mechanisms by which that plasticity proceeds at early stages, i.e., mechanisms of incipient plasticity. This discussion builds on our earlier results, reported by Li *et al.*[12] First, we summarize experimental results of nominally sharp nanoindentation for both 3D fcc crystals and a two-dimensional (2D) experimental analog. Next, we present an analytical description of elastic stability at the atomic scale in the form of the Λ criterion.

TABLE I. Experimental measurements of critical indentation load in fcc crystals.

Element	Orientation	Indenter radius (nm)	P_c (μN)	E^{*a} (GPa)	$\tau_{max}{}^b$ (GPa)	$G/2\pi$ (GPa)	Reference
Aluminum	(110)	50	30	72.6	7.2	4.36	13
	(111)	50	8	76.0	4.7	4.6	13
	(133)	50	15	63.6	5.7	4.46	13
	(113)	NA[d]	11.3	65.8		4.0	47
Copper	(111)[c]	50	35	123	10.7	7.6	46
Gold	(110)	205	7.9	117	2.5	4.6	49
	(111)	205	31.3	81.8	3.1	6.6	49
	(111)	70	14.5	117	6.2	6.6	8
	(100)	205	43.8	43	2.2	2.46	49
Iridium	(100)	50	58.5	370	26.4	34.3	50

[a]Equation (16) for $E_i = 1100$ GPa and $\nu_i = 0.07$.
[b]Equation (15).
[c]60–80 % (111) texture.
[d]Reference 48; not available.

We verify the corresponding predictions of defect nucleation and slip character with experiments and MD simulations of 2D indentation, as well as with MD and nonlinear finite element modeling (FEM) of cylindrical indentation in elastically anisotropic crystals. Finally, we present experimental results and 3D MD simulations of nominally sharp nanoindentation that reveal that, subsequent to the initial elastic instability, the development of incipient plasticity under contact loading is not due to *continued*, homogeneous nucleation of dislocations. Rather, instabilities observed beyond the first event are due to the formation of heterogeneous defect sources that operate at local stresses well below those required for homogeneous nucleation. Although our experimental and computational correlations focus on nanoscale contact, the analytical and computational tools presented herein are applicable to the general phenomenon of large strain deformation, a process relevant to a wide range of disciplines.

II. EXPERIMENTAL OBSERVATIONS

A. Nanoindentation

The results of load-controlled, nominally sharp nanoindentation experiments on several different fcc crystals have been reported, as summarized in Table I. Although these experiments were conducted on various instruments and the elastic moduli E of the crystals ranged from 69 to 528 GPa, all of the indentation responses exhibited displacement excursions beyond some critical indentation load P_c (see Fig. 1). In fact, as suggested by Gouldstone *et al.*,[13] a continuum approximation of the maximum shear stress corresponding to P_c for each crystal indicates that the first displacement excursion occurs when the Hertzian maximum shear stress τ_{max} is on the order of the theoretical shear strength of the crystal, estimated as $G/2\pi$ where G is the resolved shear modulus. This observation suggests that the local stresses prior to these discontinuities are sufficient to induce homogeneous nucleation in crystals of initially low defect density. However, this rough correlation cannot be used to rationalize subsequent displacement bursts, or to determine the initial location and structure of such homogeneously nucleated defects.

Using reliable electronic structure methods, Roundy *et al.* calculated the ideal shear strengths on {111} planes of Al and Cu to be 1.85 and 2.65 GPa, respectively, when the remaining five stress components are fully relaxed.[14] The nominal difference between the above theoretical predictions and Table I is significant, but direct comparison may not be meaningful due to the following facts. As Roundy *et al.* noted, the tangential modulus is softened significantly just prior to yielding of a crystal, causing the linear elasticity

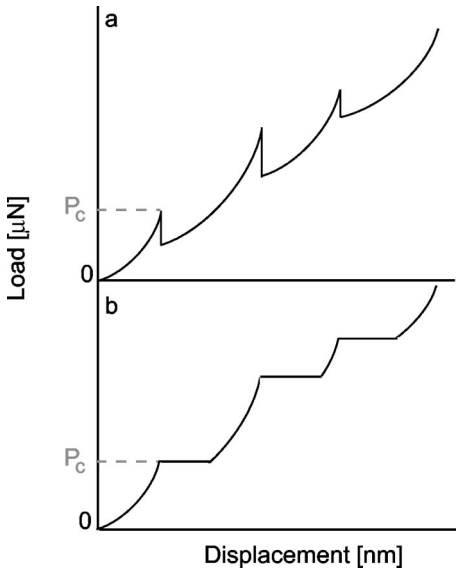

FIG. 1. Schematic of indentation load-displacement response indicating initial defect nucleation at a critical load P_c, and subsequent defect activity at increased loads and displacements. (a) Displacement control, showing sharp decreases in load (dips) corresponding to defect activity. (b) Load control, showing large increases in indenter displacement (bursts) corresponding to defect activity.

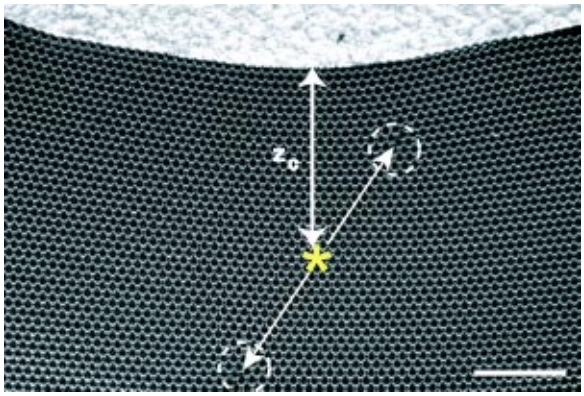

FIG. 2. (Color online) Nanoindentation normal to the terminal edge of a close-packed plane of a 2D bubble raft produces subsurface dislocation dipole nucleation. Nucleation depth z_c scales with indenter tip radius R, but the dislocation dipole structure and motion upon nucleation is invariant. The scale bar is 10 mm, or 3 nm in the atomistic size scale analogy of Gouldstone *et al.* (Ref. 16).

extrapolation[15] that Table I uses to *overestimate* the local stress at the site of homogeneous nucleation. On the other hand, the stress condition at the defect nucleation site beneath an indenter is far more complicated than the pure shear condition that Roundy *et al.* studied. Our MD calculations show that the mean pressure at the defect nucleation site is on the order of tens of GPa; therefore significant pressure-induced shear hardening is possible. These two countering factors make the comparison between the idealized electronic structure method results and the particular response under indentation-induced strains a difficult task. The resolution of this discrepancy can be mediated by a rigorous, localized elastic stability criterion that is applicable under general loading conditions.

B. Bubble raft analog

In order to visualize readily the response of atoms to localized nanoscale contact, Gouldstone *et al.*[16] employed the Bragg-Nye bubble raft model, a two-dimensional experimental analog to close-packed crystals.[17] The bubble raft provides a perfectly arranged, defect-free, 2D lattice comprising several thousands of bubbles arranged analogously to the closest-packed plane in an fcc crystal. The surface tension of the solution and the bubble diameter can be designed such that the interaction among bubbles reflects a simple description of the interatomic potential of Cu.[18] By relating the indentation-induced motion of millimeter-scale bubbles in a close-packed raft to that of nanometer-scale atoms in a close-packed atomic plane, it was shown that homogeneous dislocation dipole nucleation occurs subsurface, at the location of maximum shear stress predicted by 2D continuum contact mechanics. Further experiments confirmed that, although the depth of dislocation nucleation scales with the width of contact, the dipole structure and subsequent formation of surface steps are independent of length scales such as the indenter radius (see Fig. 2). One inherent limitation of these experiments is that the load–depth response does not converge for 2D indentation. That is, the indentation depth corresponding to a given applied load depends directly on the dimensions of the indented substrate. Thus, although it can be inferred from continuum analysis that the position of nucleation corresponds to that of the shear stress maximum, the applied stress prior to nucleation cannot be measured experimentally. For this reason, the quantitative results from nanoindentation (P_c) and bubble raft experiments (nucleation position and dislocation structure) cannot be compared directly.

III. ANALYTICAL CRITERION OF ELASTIC STABILITY

Unequivocal validation of hypotheses regarding contact-mediated instabilities requires not only precise correlation of atomic scale motion and the far-field load-depth response, but also a theoretical framework that offers predictive capabilities from which further experiments can be designed. To this end, we first review the work of Hill[19] and Rice[20] on continuum formulations of elastic stability, and then extend these concepts to the atomic scale in the Cauchy-Born framework for crystalline metals.

A. Derivation of the Λ criterion

Hill[19] developed the general concept of continuum medium stability in terms of ''acceleration waves,'' which in the context of this paper can be understood simply as long-wavelength phonons or elastic waves. He derived a tensor representing the connection between wave frequency and the corresponding wave vector $\mathbf{k}$ and displacement vector $\mathbf{w}$:[19]

$$\Lambda(\mathbf{k},\mathbf{w}) \equiv (C_{ijkl} w_i w_k + \tau_{jl}) k_j k_l , \tag{1}$$

where τ_{jl} is the Cauchy stress and C_{ijkl} is the isothermal elastic constant, defined as,[21]

$$F(Y) \equiv F(X) + \Omega(X) \left\{ \tau_{ij}(X)\, \eta_{ij} + \frac{1}{2} C_{ijkl}(X)\, \eta_{ij}\, \eta_{kl} + \cdots \right\}, \tag{2}$$

where $F(X)$ and $F(Y)$ are the Helmholtz free energies of homogeneous configurations X and Y and η is the Lagrangian strain of Y with respect to X. For a given $\mathbf{k}$, the value of $\mathbf{w}$ that gives rise to an extremum in $\Lambda(\mathbf{k},\mathbf{w})$ is the phonon eigendisplacement, and in this context Λ is proportional to the vibrational frequency squared. In the long-wavelength limit, $|\mathbf{k}|$ and $|\mathbf{w}|$ are immaterial, and hence we stipulate that

$$|\mathbf{k}| = 1, \quad |\mathbf{w}| = 1, \tag{3}$$

and hereafter $\mathbf{k}$ and $\mathbf{w}$ are used only to denote directions.

If there exists a pair of $\mathbf{k}$ and $\mathbf{w}$ such that $\Lambda(\mathbf{k},\mathbf{w})$ is negative, then the elastic stability of the homogeneous medium is lost: negative Λ signifies negative concavity of the free energy surface, and thus the frequency of the corresponding elastic wave is imaginary and its amplitude increases exponentially with time. This would ultimately result in the destruction of the homogeneous medium and the creation of defect singularities within. The growth of the ''soft mode'' wave proceeds in four stages: (i) linear growth of the unstable elastic wave, well described by continuum; (ii) nonlinear evolution at larger amplitudes, over which the wave

profile steepens; (iii) progressive steepening of the wave front until its length scale approaches atomic spacing, upon which its description must be transferred from a continuum to an atomistic basis; (iv) arrest of the atomistically sharp wave front in a low-dimensional atomic energy landscape, at which point a defect is nucleated. If the wave is transverse, the instability will likely result in the formation of a dislocation or twin of slip plane normal **k** and Burgers vector direction **w**; if the wave is longitudinal, a microcrack would likely result. The exact character of the resulting defect is a function of both the continuum-scale linear instability caused by external loading and the atomic scale interactions within the material. This dynamic process is studied in detail in another paper[22] and is, in general, complicated. Acknowledging this complexity, we make the following observations for most monatomic crystals:

(1) If the angle between **k** and **w** is greater than 60°, i.e., the initial soft mode is chiefly *transverse*, then the final defect created is likely to be a dislocation loop or a twinning embryo. The structure of the final defect should correlate strongly with whether **k** is the plane normal of a crystallographic dislocation slip system or twinning slip system.

(2) If the the angle between **k** and **w** is less than 30°, i.e., the initial soft mode is mostly *longitudinal*, then the final defect created is likely to be a microcrack.

Rice[20] derived the same stability criterion in the context of a particular continuum phenomenon, that of shear band formation. From this viewpoint, one considers an interface of normal **k** between a plastically deforming shear band and elastically deforming material, across which there is a displacement discontinuity **w**. When $\Lambda(\mathbf{k},\mathbf{w})$ becomes negative, Rice showed that traction equilibrium across the interface can no longer be maintained, and the shear band thus grows catastrophically. Although the nomenclature and articulation of the criterion formulated by Hill and Rice contrast slightly, they are entirely equivalent in content. Mathematically, this criterion can be summarized as

$$\Lambda_{\min} \equiv \min_{|\mathbf{k}|=1,\ |\mathbf{w}|=1} (C_{ijkl} w_i w_k + \tau_{jl}) k_j k_l , \tag{4}$$

and if $\Lambda_{\min}$ is negative, the specific material point or representative volume element (RVE) becomes elastically unstable.

A full phonon spectrum analysis of a strained crystal can be carried out; this has been performed for binary compounds such as SiC.[23] Such calculations show the connection between Brillouin zone boundary soft phonons and the ideal strength of these systems. Indeed, because the phonons constitute a complete basis set for all atomistic excitations in a crystal, such analysis is *necessary and sufficient* to ascertain the stability of any crystal at $T=0$. The present elastic wave analysis, however, does not guarantee stability: It is a necessary condition. Despite this lack of sufficiency, the concept and implementation of the Λ criterion are extremely powerful and cover the majority of instabilities that occur in monatomic crystals. The fact that Eq. (1) is a tractable analytical formula involving only well-known mechanical parameters τ_{ij} and C_{ijkl}, which are also well studied in atomistic simulations,[24] makes it an ideal means to connect continuum models such as FEM with atomistic simulations. Additionally, as the Λ criterion relies on the long-wavelength limit and thermoelastic material response, it continues to function at finite temperatures, when the phonon description loses its rigorous definition. We will demonstrate that in realistic loading configurations such as nanoindentation, Eq. (1) correctly predicts the critical load and the defect nucleation site. In addition, this energetic criterion reasonably predicts the character of the defect when we combine information about the soft mode **k** and **w** with crystallographic structure. That is, we can predict whether the linear instability will lead to a dislocation loop or a twinning embryo, specifying the slip plane and the Burgers vector. This allows true predictive power in finite-element models, afforded by a *defect nucleation criterion* with no adjustable parameters for a given description of atomic interactions.

B. Incorporation of the Λ criterion into computational analyses

Two practical difficulties prevented the Λ criterion, formulated at the continuum scale several decades ago, from being widely used in practice. The first challenge is the lack of accurate constitutive models to estimate τ_{ij} and C_{ijkl} at *very large strain*, near elastic instabilities. The parametrization of the strain energy function or stress functions in six-dimensional general strain space is by no means a simple task, either conceptually or numerically. Prior to the advent of modern, reliable electronic struture codes and their derivative empirical interatomic potentials, few data existed. Another obstacle is the accurate calculation of $\Lambda_{\min}$. Even though four-dimensional minimization (since $|\mathbf{k}|=1$, $|\mathbf{w}|=1$) is not an especially difficult computation to perform a single time, a reliable and efficient algorithm is necessary due to the iteration of this procedure for each material point. For example, in the context of MD, the calculation of $\Lambda_{\min}$ is performed for each of up to 2×10^6 atoms at each time step.

The first challenge can be resolved naturally in an atomistic calculation because one can conceptualize and evaluate atomistic local stress τ_{ij} and atomistic local elastic constant C_{ijkl} by partitioning the virial and Ray sums,[25,24] respectively, down to individual atoms. For pair and embedded-atom type interatomic potentials, such partitioning is straightforward because the total virial and Ray sums are comprised algebraically of contributions from atom pairs, and one can readily attribute half of every pair contribution to each of the two participating atoms. More complicated interatomic formulations and partitioning schemes[26] would work equally well, provided that basic symmetry and sum rule requirements are satisfied. This partitioning scheme is justifiable insofar as the atom under consideration is a few atomic spacings away from any topological defects, even if it is under a large elastic strain. In other words, as long as several nearest-neighbor levels of an atom retain their (bulk) crystalline coordination, the concept of atomistic local stress and elastic constant is well posed and one can evaluate them directly from an interatomic potential, or even from *ab initio* calculations.

To overcome the second difficulty, we observe that $\Lambda(\mathbf{k},\mathbf{w})$ is a biquadratic function in $\mathbf{w}$ and $\mathbf{k}$, and can be alternatively written as

$$\Lambda(\mathbf{k},\mathbf{w}) \equiv (C_{ijkl}k_jk_l)w_iw_k + \tau_{jl}k_jk_l, \tag{5}$$

where the order of the $\mathbf{k},\mathbf{w}$ summation is swapped from Eq. (1). If we assume $\mathbf{w}$ is a constant in Eq. (1) and minimize against $\mathbf{k}$ only, then the solution for that simple quadratic form is straightforward: Diagonalize the 3×3 symmetric matrix $[\mathbf{A}]_{jl} \equiv C_{ijkl}w_iw_k + \tau_{jl}$ and choose the softest eigenvector to be $\mathbf{k}$. Alternatively, if we assume that $\mathbf{k}$ is a constant in Eq. (5) and minimize against $\mathbf{w}$, then the solution is also straightforward: Diagonalize the 3×3 symmetric matrix $[\mathbf{B}]_{ik} = C_{ijkl}k_jk_l$ and choose the softest eigenvector to be $\mathbf{w}$. Therefore, we propose the following iterative algorithm to minimize $\Lambda(\mathbf{k},\mathbf{w})$:

(a) Choose an arbitrary $\mathbf{w}$.

(b) Minimize Eq. (1) for a fixed $\mathbf{w}$, identifying an initial value of $\mathbf{k}$ that minimizes $\Lambda(\mathbf{k},\mathbf{w}_{\text{fixed}})$.

(c) Minimize Eq. (5) for a fixed $\mathbf{k}$ identified in the previous step, identifying an initial value of $\mathbf{w}$ that minimizes $\Lambda(\mathbf{k}_{\text{fixed}},\mathbf{w})$.

(d) Repeat until mutual convergence is reached.

The above uses only 3×3 symmetric matrix diagonalization, which can be implemented efficiently using the analytical, Cardano cubic equation solution.[27]

Using the approaches outlined above, a complete recipe for Λ criterion implementation in atomistic simulations is proposed:

(1) Select all atoms sufficiently separated from topological defects, even if they are withstanding large elastic strain.

(2) Evaluate the local atomistic stress and elastic constant on an atom-by-atom basis by distributing the virial and Ray sums.[25,24] This allows $\Lambda(\mathbf{k},\mathbf{w})$ to be properly defined for each atom.

(3) Minimize $\Lambda(\mathbf{k},\mathbf{w})$ for each atom, and record $\Lambda_{\min}$, $\mathbf{k}$, and $\mathbf{w}$ for each atom. $\Lambda_{\min}$ can be interpreted as the *microstiffness* of the atom, and its sign can be interpreted as the concavity of the free energy F.

(4) Among all atoms in the configuration, identify the atom with the smallest $\Lambda_{\min}$ as the ''softest atom'' for the particular displacement configuration.

Despite the large number of atoms in a typical 3D MD simulation of nanoindentation ($\sim 2\times10^6$), the efficiency of the above minimization procedure is sufficient to allow simultaneous simulation and calculation of $\Lambda_{\min}$. At the onset of homogeneous nucleation, $\Lambda_{\min}$ of the ''softest atom'' tends to zero. Note that the Λ criterion does not force $\mathbf{w}$ and $\mathbf{k}$ to correspond to close-packed directions and planes. Rather, correspondence of $\mathbf{w}$ and $\mathbf{k}$ to $\langle 110\rangle$ and $\langle 111\rangle$, respectively, in the 3D simulations discussed below is a natural outcome of the interatomic potential within the fcc crystal structure.

Because instabilities predicted by the Λ criterion are elastic in nature,[21] and since all atomic information is incorporated through C_{ijkl} and τ_{ij}, this defect nucleation criterion also can be readily incorporated within finite-element analysis. Such implementation requires that (i) the large strain formalism be used (e.g., the nonlinear geometry option in a general purpose finite-element package such as ABAQUS[28]) and (ii) an accurate constitutive relation be provided to the finite-element code. The latter is facilitated by the model of Cauchy-Born elasticity by which the local stress state at a material point is dictated by the movements of underlying lattices.[29,30] Specifically, FEM-imposed boundary conditions cause displacement of the nodes. The stress at each node is calculated in a subroutine comprising a small atomic lattice for which the lattice interaction is determined by an interatomic potential (i.e., molecular statics at $T=0$ and ensemble averaging at finite T). When this lattice is strained according to the FEM nodal displacement, interatomic interactions dictate stresses on each atom according to the potential, giving a local (nodal) value of τ_{ij}. Both C_{ijkl} and τ_{ij} can be calculated through manipulation of Eq. (2). The quantity $\Lambda(\mathbf{k},\mathbf{w})$ can also be calculated and minimized for each node, according to the procedure outlined above. In this manner, the deformation of large-scale models can be dictated by an essentially atomic scale strain-to-failure criterion; this criterion is parameter-free for a given interatomic potential. As the constitutive response of this FEM approach is dictated by interatomic potential (IP), we will refer to it hereafter as IPFEM. Although IPFEM is not the first computational approach that allows observation of defect nucleation, this model represents the first framework that incorporates a *predictive*, local elastic stability criterion that is directly linked to defect nucleation.

IV. COMPUTATIONAL MODELING OF ELASTIC STABILITY

Computational simulations such as MD are particularly well suited to quantify the relationship between internal atomic activities and external loading sustained by a crystal: The only assumption of material behavior in MD is that a certain interatomic potential correctly describes the interaction among atoms. However, due to the computational cost associated with keeping track of large numbers of atoms, the physical time scales and/or length scales are often unrealistically small. By contrast, continuum-based computational approaches such as FEM are, by definition, designed to simulate behavior over any length scale for which the material response can be described by continuum parameters (e.g., Young's modulus E and yield strength σ_y). The objective of IPFEM, then, is to incorporate the accuracy and parameter-free nature of MD and related simulations into the realistic length and time scales of FEM.

IPFEM is distinct from the quasicontinuum (QC) method[31] in that it does *not* transfer the basis of the material description from continuum-based elements to atomistic-based MD when the elemental response approaches the elastic limit. Rather, IPFEM is a fully continuum finite-element model at *all* levels of strain, for which the nodal response of crystalline RVEs is governed by an atomistic (Cauchy-Born) constitutive relation.[29] In contrast, QC hybridizes the use of linear and Cauchy-Born nonlinear elasticity with MD, transferring the constitutive relations according to the level of local strain, and thus utilizes a numerical, rather than analytical, nucleation criterion. The fields calculable via IPFEM

are, by design, easily integrated with the $\Lambda(\mathbf{k},\mathbf{w})$ analysis tool. As such, IPFEM is conceptually less general than the quasicontinuum method and can handle only a subset of the problems the quasicontinuum method is theoretically capable of treating, for which the results of the two methods should be largely the same. That is, although the quasicontinuum method can be used to identify and validate a defect nucleation criterion, to our knowledge the quasicontinuum method has not been applied to this task. Three considerations lead us to think that IPFEM is sufficiently important and unique to be identified separately from the general quasicontinuum method:

(1) Difference in perspective: We do not regard the small atomic lattice in question as being embedded in a larger, inhomogeneously strained atomic configuration. Instead, we consider the small atomic lattice to be embedded in an infinite, but homogeneously strained lattice, representing a material point in the FEM calculation. This more ''primitive'' viewpoint enables modular design. That is, we can couple FEM to either interatomic potential or to more accurate *ab initio* periodic boundary condition (PBC) unit-cell calculations.[32] Although the incorporation of *ab initio* constitutive descriptions is not a large advance conceptually, this ability would have great practical impact with respect to reliability and accuracy of observations and predictions made at the atomic scale.

(2) Ease of implementation: One may utilize any general-purpose FEM package such as ABAQUS to implement IPFEM, simply by supplying the appropriate constitutive relation. Thus, IPFEM requires no modification of the meshing, visualization, and analysis tools, whereas the general quasicontinuum method requires significant effort to code and implement.

(3) Dedication to an important phenomenon: The special set of problems that IPFEM can study, e.g., the site and character of homogeneous nucleation occurring in nanoindentation, is sufficiently important and underdeveloped that a simple method that achieves this goal with minimal effort should be promoted. As one cannot truly separate a method from the problems it can solve, IPFEM is, by design, linked to application of the Λ criterion and the general phenomenon of homogeneous defect nucleation.

In this section, we discuss prediction of elastic instability via the Λ criterion for both MD and IPFEM simulations of nanoindentation in two- and three-dimensional crystals.

A. MD simulation of indentation on a 2D half plane

In order to verify the assumptions and implementation of the Λ criterion, we conducted 2D MD simulations of the bubble raft experiments outlined in Gouldstone *et al.*[16] As we are not interested in the mechanical response of an actual soap bubble raft, but instead regard it as a generic model of close-packed 2D crystals, we arbitrarily choose the following potential with a smooth, short-range cutoff for ease of implementation,

$$V(r)=\begin{cases}\alpha(r-1)^4-\beta(r-1)^2, & r<1\\ 0, & r\geqslant 1\end{cases} \tag{6}$$

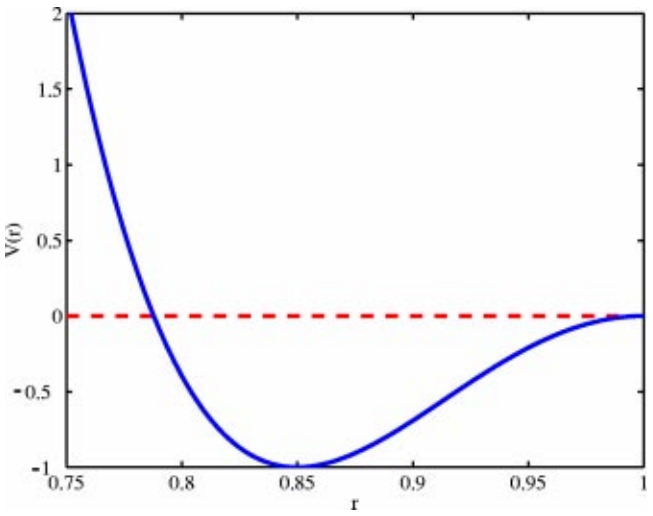

FIG. 3. (Color online) Generic short-ranged interbubble potential with equilibrium separation distance $r_0=0.85$. Both the potential well depth and cutoff distance are set to unity and serve as normalizations of energy and length, respectively. This potential was used in molecular dynamics simulations of the bubble raft, our model 2D system.

which is plotted in Fig. 3. Here, the primary units of length and energy are the cutoff distance r_c at which the potential is valued zero and potential well depth ϵ, respectively, and are both scaled to 1. Consequently, a single parameter r_0, the equilibrium interbubble distance, controls the shape of the potential for any interbubble distance $r\leqslant r_c$. We normalize this distance by r_c valued unity, so that r_0 is a dimensionless quantity less than unity. In order to convert from these normalized values to physical units in actual experiments, one multiplies normalized quantities by physical measures of ϵ and r_c (e.g., critical load of value P, multiplied by $\{\epsilon/r_c\}=\{1.55\ \text{J}/0.003\ \text{m}\}$, to obtain force in N). We express the quantities that modulate the potential, α and β, as

$$\alpha=(1-r_0)^{-4},\quad \beta=2(1-r_0)^{-2}. \tag{7}$$

We observe more brittle behavior at larger r_0. In all the following results, r_0 is taken to be 0.85, and plots of potential and depth are shown in these reduced units. At equilibrium, the potential energy per bubble is -3, the volume per bubble is $\Omega_0=\sqrt{3}r_0^2/2$. At equilibrium, the raft is an isotropic elastic medium with elastic constant matrix,

$$\mathbf{C}=\begin{pmatrix}\lambda+2\mu & \lambda & 0\\ \lambda & \lambda+2\mu & 0\\ 0 & 0 & \mu\end{pmatrix}, \tag{8}$$

whereby the fourth order C_{ijkl} tensor is reduced to a 3×3 matrix due to symmetry in an isotropic elastic system in which Voigt indices 1,2,3 denote xx,yy,xy stress/strain components, respectively. The strain energy per bubble at uniform Lagrangian strain η is

$$E = 3 + V\{r_0\sqrt{[1,0](1+2\eta)[1,0]^T}\} \times V\{r_0\sqrt{[1/2,\sqrt{3}/2](1+2\eta)[1/2,\sqrt{3}/2]^T}\} + V\{r_0\sqrt{[-1/2,\sqrt{3}/2](1+2\eta)[-1/2,\sqrt{3}/2]^T}\}. \quad (9)$$

Using the fact that $V'(r_0)=0$, we may expand the above as

$$E \approx \frac{V''r_0^2}{2}\left[\eta_{xx}^2 + \left(\frac{\eta_{xx}}{4} + \frac{\sqrt{3}\,\eta_{xy}}{2} + \frac{3\,\eta_{yy}}{4}\right)^2 + \left(\frac{\eta_{xx}}{4} - \frac{\sqrt{3}\,\eta_{xy}}{2} + \frac{3\,\eta_{yy}}{4}\right)^2\right] = \frac{V''r_0^2}{2}\left[\frac{9\,\eta_{xx}^2}{8} + \frac{3\,\eta_{xx}\eta_{yy}}{4} + \frac{9\,\eta_{yy}^2}{8} + \frac{3\,\eta_{xy}^2}{2}\right], \quad (10)$$

from which we can derive that

$$C_{11}=C_{22}=\frac{9V''r_0^2}{8\Omega_0}, \quad C_{12}=\frac{3V''r_0^2}{8\Omega_0}, \quad C_{33}=\frac{3V''r_0^2}{8\Omega_0}, \quad (11)$$

or if we substitute

$$V''(r_0)=12\alpha(r_0-1)^2-2\beta=\frac{8}{(1-r_0)^2}, \quad (12)$$

we obtain

$$\lambda=\mu=\frac{2\sqrt{3}}{(1-r_0)^2}, \quad (13)$$

and the Poisson's ratio is therefore 1/3. When we define the equilibrium separation distance $r_0=0.85$, we obtain $\lambda=\mu=153.96$; this value of μ under zero far-field applied loading is the value of $\Lambda_{\min}$. Any shear wave with $\mathbf{k}\perp\mathbf{w}$ minimizes $\Lambda(\mathbf{k},\mathbf{w})$ equally well, with no preference along crystallographic directions, *prior to the application of far-field loading*.

The indenter is implemented as an external potential on the bubbles,

$$V_{\text{ext}}(r)=\begin{cases}\exp\left(\dfrac{R-r}{d}-\dfrac{d}{R-r}\right), & r<R\\ 0, & r\geqslant R,\end{cases} \quad (14)$$

where r is the distance between any bubble to the origin of the indenter, R is the indenter radius, and d is the indenter hardness, representing the distance over which a bubble can (numerically) penetrate the indenter potential. As such, there is zero friction between the indenter and the substrate. $V_{\text{ext}}(r)$ increases from 0 infinitely smoothly upon contact, but rises precipitously when the bubble is $\sim d$ inside the indenter, representing practically a very hard indenter.

Two simulation algorithms have been used: molecular dynamics at $T=0$ K and conjugate gradient minimization. In molecular dynamics simulations, the bubble mass is arbitrarily chosen to be 1. For equilibrium interbubble distance $r_0=0.85$, Eq. (12) shows that the stiffness constant is on the order of 400. Therefore $\nu_{\max}$, the maximal oscillation frequency, is ~ 3. We use the six-value Gear predictor-corrector algorithm[33] to integrate the trajectory of atoms moving on the interatomic potential surface, with an integration time step of 0.003, corresponding to about 100 force evaluations per period for the hardest oscillation, ensuring numerical stability. The thermostat scheme[34] of Berendsen *et al.* is used, with the temperature-coupling time constant chosen to be 3, making the system strongly dissipative such that vibrations due to kinetic energy are quickly restored to the level designated by the specified temperature; this minimizes reflection of oscillations from boundary conditions. At the beginning of a simulation, the indenter is placed such that its perimeter exactly touches the first row of bubbles, the indenter force is initially zero but it increases immediately upon penetration. The bottom layer of bubbles is fixed, constraining the raft to be deformed by the indenter. PBCs are used in the x direction (in-plane). In the MD simulation, the indenter proceeds in displacement control, moving toward the substrate by a small, fixed increment every time step. In the conjugate gradient minimization, the indenter advances by 0.02 every step, after which the entire raft of bubbles is relaxed except for the bottom layer, so the net force on each bubble is zero. In both simulations, the force $V_{\text{ext}}(r)$ exerted on the bubbles is summed and is correlated with the indenter displacement. We found it more advantageous computationally to explore the general phenomenon using molecular dynamics with smaller bubble rafts of thousands of bubbles. However, in order to verify the Λ criterion with maximum accuracy, we utilized conjugate gradient minimization on larger bubble rafts comprising $\geqslant 100\,000$ bubbles.

Figure 4 shows the change in far-field indentation load and $\Lambda_{\min}$ as a function of imposed indenter displacement for a 2D MD simulation comprising 112 400 bubbles. The indenter is cylindrical with radius R of 160, d of 0.8, and the interatomic potential is given by Eq. (6). The critical indentation depth for the first homogeneous defect nucleation event is 14.84, in reduced units; conversion to physical units requires multiplication of this value by a real cutoff length r_c. The temporal correspondence of discontinuous load relaxations and the vanishing of $\Lambda_{\min}$ is excellent for the first load discontinuity, and the same trend is observed for five subsequent discontinuities. Through visualization of the atomic coordination number, we have verified that each load relaxation corresponds exactly with the nucleation of one dislocation dipole. This result indicates that the Λ criterion can predict accurately the far-field load and displacement conditions that will induce defect nucleation in a perfect crystal. If atoms that comprise the nucleated defects are not removed numerically from the minimization procedure—equivalent to removing the dislocation core from an elastic analysis—$\Lambda_{\min}$ attains negative values. Of course, this transition to negative values does not indicate a new material response or a negative microstiffness within the crystal. In fact, this merely reflects the fact that one fundamental assumption of the above elastic stability analysis, namely, that the indentation strain field is homogeneous, breaks down in the neighborhood of under- and overcoordinated atoms that comprise defects. In other words, the Λ criterion predicts the

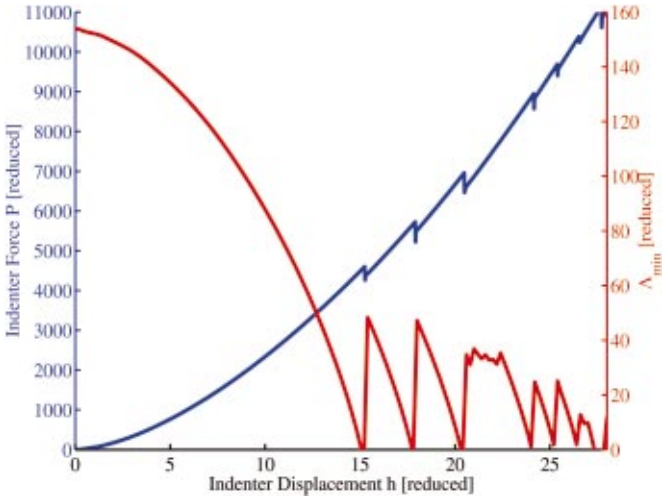

FIG. 4. (Color) MD simulation of indentation of an initially elastic-isotropic close-packed plane, using the interbubble potential. Indentation load P and $\Lambda_{\min}$ are shown as a function of imposed indentation depth h. $\Lambda_{\min}$ is identically zero for each load relaxation, each of which corresponds exactly to the homogeneous nucleation of a dislocation dipole at the site within the crystal of minimum $\Lambda_{\min}$.

conditions for *homogeneous* defect nucleation. Thus, the applicability of this stability analysis is restricted to regions of perfect crystallinity under elastic deformation.

Figure 5(a) shows the von Mises stress invariant distribution in the bubble raft just prior to the elastic instability. We find that the maximum von Mises stress does not occur along the central loading axis but is distributed off-axis by 16.5 on both sides, at which point the stress is 20.97. In contrast, Fig. 5(b) shows that the minimum $\Lambda_{\min}$ does indeed occur along the loading axis, at a depth greater than that corresponding to maximal von Mises stress. Figure 5(c) shows τ^{Mises}, τ^{resolved}, $\tau^{\text{continuum}}$, and $\Lambda_{\min}$ in reduced units, along the central loading axis. As $\tau^{\text{Mises}}_{\max}=20.26$, this maximum shear stress does not deviate significantly from the absolute maximum that occurs off-axis. More importantly, the homogeneous dislocation site corresponds exactly with the position of minimal $\Lambda_{\min}$, not with the position of maximum shear stress. Thus, the *microstiffness* prediction of the elastic limit embodied by the Λ criterion describes the defect nucleation site more accurately than a stress-based criterion such as $\tau^{\text{Mises}}_{\max}$.

The soft **k** calculated by the Λ criterion agrees perfectly with the nucleated dislocation glide plane normal, which is aligned to a crystallography orientation. However, the calculated soft **w** differs from the actual Burgers vector by $\sim 12°$. This results from an activation volume effect, whereby the instantaneous slip direction at the saddle differs from the full slip direction due to the in-plane, corrugated potential profile over which a migrating atom must slide over.

B. Comparison of MD and IPFEM for cylindrical indentation

We conducted simulations of cylindrical nanoindentation via MD and IPFEM in order to compare these approaches and verify the slip character of the homogeneously nucleated

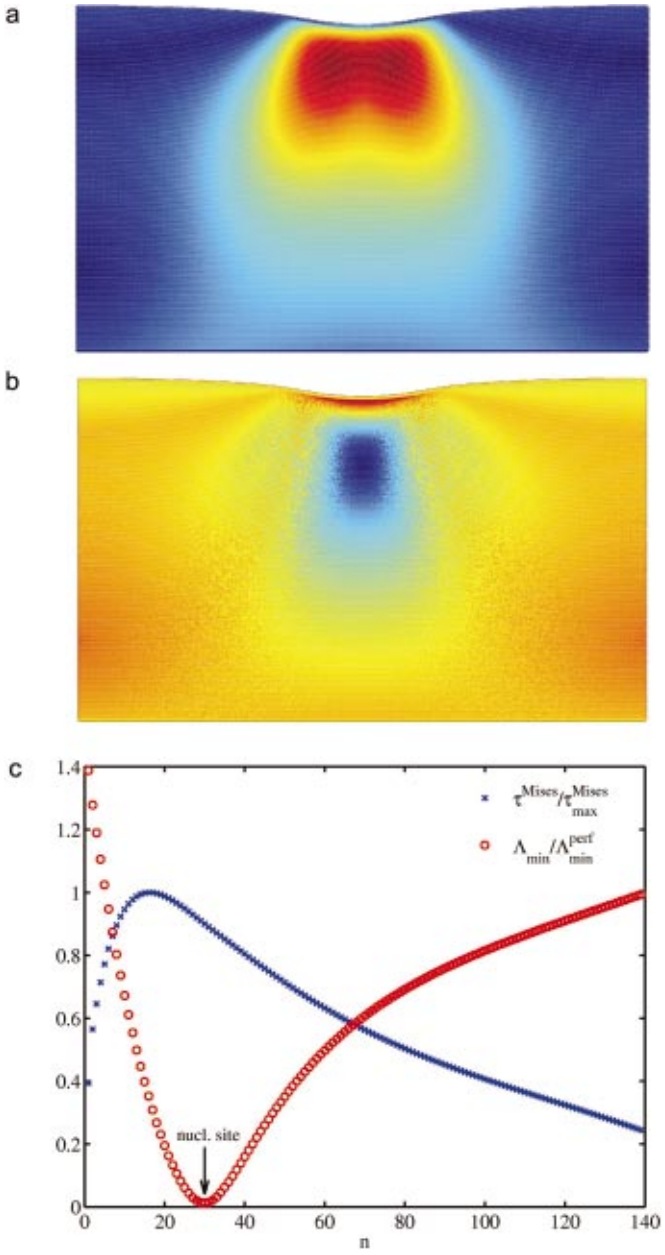

FIG. 5. (Color) Distribution of (a) von Mises stress invariant in the MD simulation of the 2D bubble raft, just prior to defect nucleation. The position of maximum τ (dark red) does not correspond exactly with the defect nucleation position. (b) $\Lambda_{\min}$ in the same simulation shows the global minimum of the energetic criterion along the loading axis (dark blue), at a position corresponding exactly with the point of defect nucleation. (c) Stress and $\Lambda_{\min}$ along the central loading axis. As the interparticle potential in Eq. (6) is an arbitrary and scaled model, the magnitudes of τ and Λ are not shown.

dislocations predicted by the Λ criterion. Here, we discuss results for single-crystal copper, a significantly elastic-anisotropic fcc metal. The Ackland interatomic potential[35] for Cu was used in both simulations, and displacement-controlled nanoindentation was simulated with an indenter radius of 20 nm. The Cu single crystal constructed for MD simulations, comprising 290 304 atoms and in-plane periodic

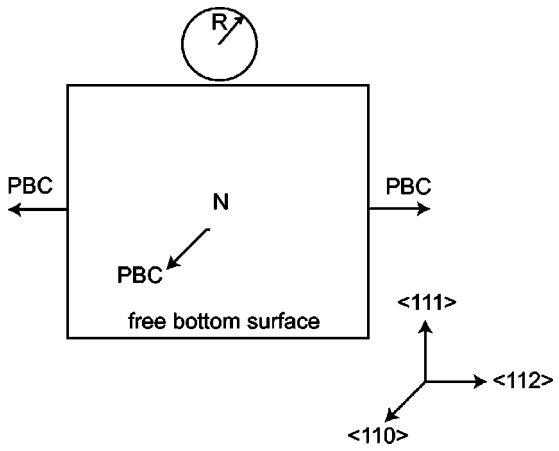

FIG. 6. Schematic of MD simulation setup used for both cylindrical and spherical indentation. For quasi-2D cylindrical indentation of Cu: $74.4\times65.1\times1.02$ nm, $168\times72\times4$ unit cells, 290 304 atoms, $D=40$ nm, $\dot{h}=27$ m/s; for 3D spherical indentation of Cu: $20.7\times19.1\times20.5$ nm, $42\times18\times72$ unit cells, 326,592 atoms, $D=13$ nm, $\dot{h}=3.5$ m/s. In both cases, $x=\langle 11\bar{2}\rangle$, $y=\langle 111\rangle$, $z=\langle 1\bar{1}0\rangle$.

boundary conditions, is illustrated schematically in Fig. 6. The crystal, comprised of $168\times72\times4$ unit cells, was free to displace along the loading axis in the y direction, as well as in the x and the out-of-plane z directions. This freedom of movement in the y direction was restrained by requiring that the load P imposed by the indenter be countered by an opposite response of $-P/N$ body force distributed equally among all atoms, where N is the total number of atoms in the simulation.

Figure 7(a) shows the position and slip character of the first dislocation nucleation event, as indicated by a decrease in atomic coordination number of the interior atoms. Although the defect is similar in structure to the edge dislocation dipoles observed in true 2D bubble raft experiments, the position of nucleation is displaced from the loading axis, and occurs nearer the surface than predicted by continuum analyis of cylindrical indentation in isotropic media ($z=0.78a$).[15] This shift of the dislocation nucleation position is due to the elastic anisotropy of Cu. Using the recently developed linear elastic Stroh anisotropic analytical solution of the cylindrical punch indentation problem,[36] we have verified[30] that the site of the maximum von Mises stress is indeed off-center by 20% and nearer to the surface ($z=0.64a$) than the isotropic solution, corresponding qualitatively with the position identified via MD.

1. Interatomic potential finite element modeling

Figures 7(b) and 7(d) show the point of elastic instability in an IPFEM simulation, using the above indentation configuration and interatomic potential. The positions of maximum effective (von Mises) stress and maximum resolved shear stress, both based on linear elastic analyses, do not coincide exactly with the position of minimum $\Lambda_{\min}$ at the point of defect nucleation. Not surprisingly, the position of maximum resolved shear stress correlates more closely with the position of minimum $\Lambda_{\min}$. More importantly, defect nucleation occurs at the point where $\Lambda_{\min}$ is exactly zero, indicating that the energetic criterion represented by $\Lambda_{\min}$ captures the elastic instability much more accurately than a stress-based approach. In other words, this result shows that the Λ criterion is a more accurate predictor of defect nucleation position, and the only predictor of defect character.

In this model, each node represents an infinite lattice under homogeneous strain; nodal points need not be concurrent with crystallographic lattice positions. Rather, the crystallographic information describing the simulated material is contained in the constitutive relation input by the user. Thus, IPFEM does not resolve a single dislocation, but instead a shear band indicating the slip orientation of such a dislocation. The shear band shown in Fig. 7(b) is identical in position and slip character to the individual dislocation observed via MD. The resulting lack of symmetry in the nucleation event indicates that the elastic anisotropy of the interatomic potential was accurately reflected for otherwise symmetric boundary conditions. In addition, the critical load at which the elastic instability occurs is identical in MD and IPFEM. These correlations verify the application of the Λ criterion to predict the conditions for and slip character of elastic instabilities in computational methods heretofore limited to continuum analysis.

C. Three-dimensional analysis of the elastic limit

We conducted 3D MD simulations of spherical indentation in Al (Ercolessi-Adamssi potential[37]) comprising 326 592 (and also up to 2×10^6) atoms, for a sphere of 13 nm radius indented normal to the {111} plane in displacement control. In all simulations, the initiation of dislocation activity was concurrent with far-field indentation load relaxation, and the dislocation structure comprised a dislocation glide loop on a {111} slip plane.

The initial load relaxation indicated in Fig. 8(a) was due to the subsurface, homogeneous nucleation of a defect embryo on a {111} plane. The nucleation site shown in Fig. 8(b) was located at a depth z equal to 51% of the contact radius a, in good agreement with the depth of $0.48a$ predicted by Hertzian (continuum) analysis of spherical contact,[15] but was located at a significant distance from the loading axis. The linear elastic solution for maximum shear stress corresponding to this load can be calculated as[15]

$$\tau_{\max}=0.31\left(\frac{6PE^{*2}}{\pi^3R^2}\right)^{1/3}, \tag{15}$$

where P is load, E^* is the reduced Young's modulus, which accounts for elastic deformation of both the indenter and the sample:

$$\frac{1}{E^*}=\left\{\left(\frac{1-\nu_{\text{indenter}}^2}{E_{\text{indenter}}}\right)+\left(\frac{1-\nu_{\text{specimen}}^2}{E_{\text{specimen}}}\right)\right\}, \tag{16}$$

and is equivalent to the Young's modulus of Al in this particular case of a completely rigid indenter, and R is the indenter radius. Just prior to dislocation nucleation, the load

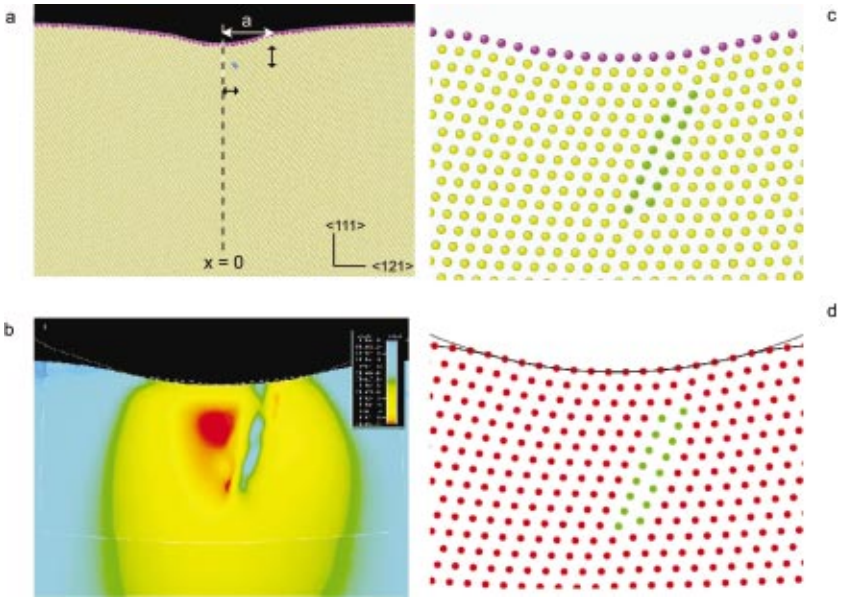

FIG. 7. (Color) Computational simulations of cylindrical indentation in Cu. (a) MD shows the dislocation dipole nucleation displaced off the loading axis. The atom color indicates coordination number *N*: yellow and pink denote perfect bulk and surface *N*, respectively; blue denotes imperfect bulk *N*, the defect site. (b) IPFEM shows a shear band of the same position and orientation indicated by MD. (c) MD shows the dislocation dipole core displaced off the central loading axis. The atom color indicates *N*: Green denotes imperfect bulk *N*. (d) Coding of IPFEM output such that each visible node corresponds to an atomic lattice site showing that the position and orientation of defect nucleation are identical to those observed in MD simulations. Atom color indicates *N*: Green denotes imperfect bulk *N*.

imposed by the 13 nm diameter indenter was 20 μN, indicating a corresponding Hertzian maximum shear stress of 3.41 GPa. Interestingly, this calculated value of Hertzian shear stress is in excellent agreement with the ideal shear strength of 3.4 GPa obtained via pseudopotential electronic structure calculations for Al in the absence of elastic relaxation.[38]

V. MECHANISMS OF INCIPIENT PLASTICITY

Next, we discuss the atomic scale activity subsequent to the onset of elastic instability. When such a dislocation nucleation and interaction process comprises approximately hundreds of dislocations, it represents the earliest stages of gross plasticity. This process is hereafter referred to as incipi-

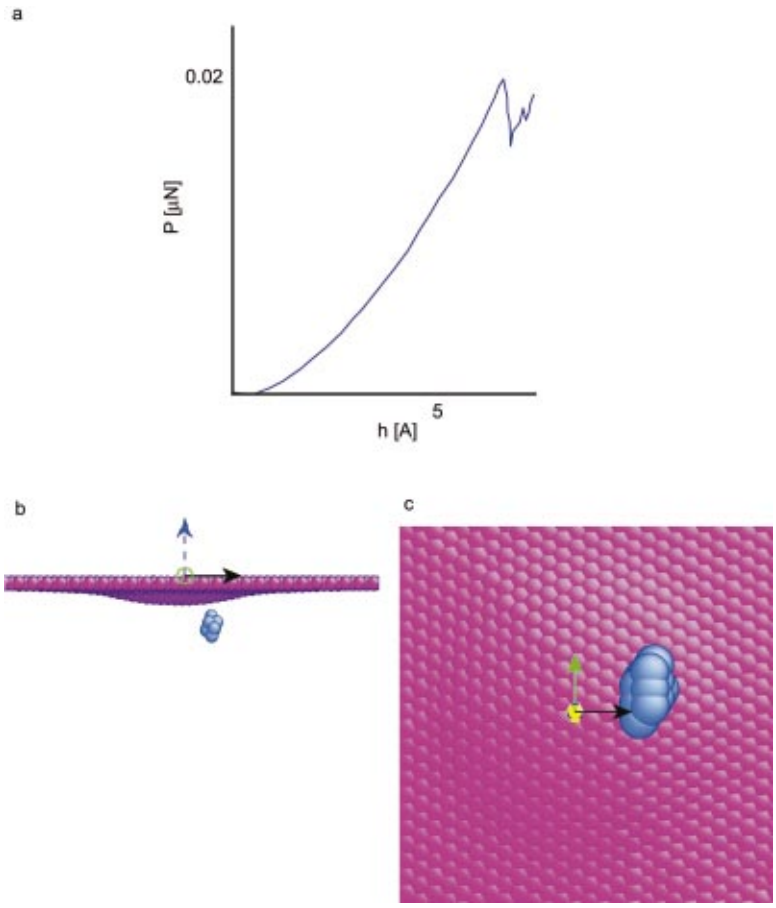

FIG. 8. (Color) Homogeneous defect nucleation in Al. (a) Indentation response to the point of initial load relaxation. (b) Corresponding atomic structure, indicating subsurface homogeneous dislocation nucleation at a depth $z = 0.51a$, where z and a are depth and contact radius, respectively. (c) Plan view from within the crystal, oriented along the loading axis toward the free surface, showing significant displacement of the nucleation site with respect to the central loading axis. Atom color indicates coordination number *N*: pink denotes perfect surface *N*; blue denotes imperfects bulk *N* (defect site); invisible bulk atoms denote perfect bulk *N*.

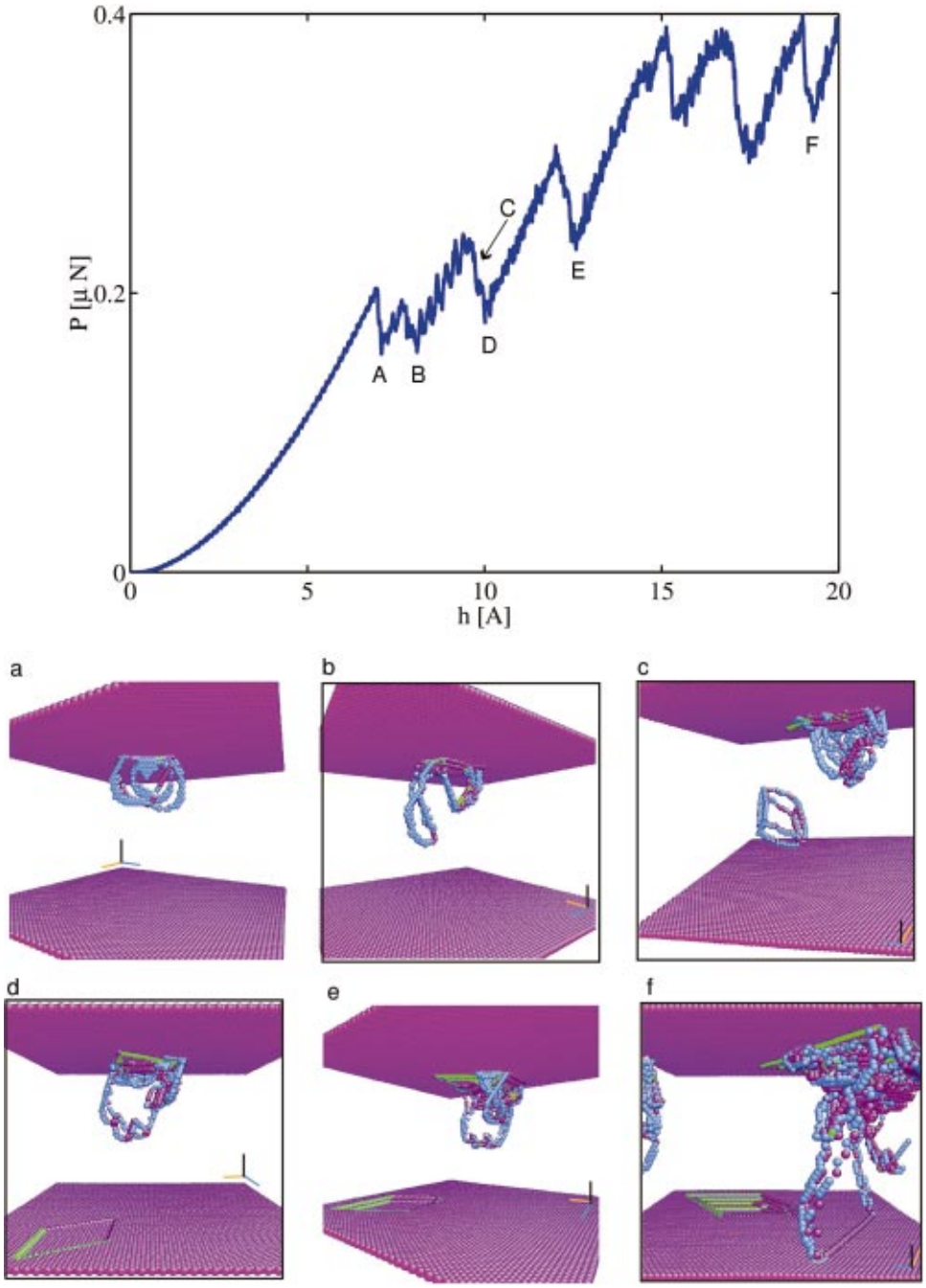

FIG. 9. (Color) Correlation of the MD indentation response and atomistic activity in Al. At several displacement increments, atoms with coordination number different from 12 are drawn.

ent plasticity, a term suggested in this context by Tadmor *et al.*[39] First, we relate the dislocation structures and mechanisms observed in 3D MD simulations of spherical nanoindentation in Al and Cu. Then, we correlate these findings with results from nominally sharp nanoindentation experiments in Al single crystals.

A. MD observations

Figure 9 correlates atomistic activity with external loading in simulations of nanoindentation for Al. Figure 9(a) shows the internal defect structure subsequent to the homogeneous nucleation event, at the conclusion of the first load relaxation. Immediately following this homogeneous nucleation event, further load relaxation was mediated by expansion of glide loops on the {111} plane [Fig. 9(b)]. Upon continued loading, the intersection of these glide loops with the surface formed a ⟨110⟩ slip step from which cross-slip onto a new {111} plane ensued [Fig. 9(c)]. A sessile lock would be formed when two loops on different {111} planes intersect. Several subsequent cross-slip events produced two parallel sets of dislocation segments, each having two partials separated by a stacking fault and pinched together at four vertices forming a prismatic loop, which mediates further load relaxation via easy motion along its glide prism [Figs. 9(c) and 9(d)]. Continued loading resulted in the formation of several more prismatic loops emanating from the same source, and then finally the formation of a prismatic loop from a different

surface source with its own glide prism oriented 120° from the first source [Fig. 9(e)]. The observed interaction of surface steps and subsurface dislocation is similar to the concept of a defect complex hypothesized by Cleri *et al.* in the context of crack-tip plasticity.[4]

The initial stage of dislocation activity following the elastic instability in Al is likely to result in the formation of a sessile dislocation structure. We have confirmed with simulations of up to 2×10^6 atoms that the above-said structure and associated surface steps tend to be threefold symmetric, consistent with the threefold symmetry of available $\{111\}\langle110\rangle$ slip systems of the fcc crystal for the $\langle111\rangle$ indentation direction. Because such atomic-scale inhomogeneities are *unable* to move away from the high local stress region, subsequent dislocation nucleations are likely to be thermally activated and heterogeneous process. Additionally, our observations indicate that these secondary products—the prismatic loops—tend to be much more mobile than the first set of glide dislocation loops since they move outward and do not interfere with one other, and are able to move all the way down to the substrate without impedance.

Identical 3D MD simulations of nanoindentation in Cu indicated that partial dislocation loops are nucleated at a load corresponding to the theoretical shear strength of Cu. The glide loops formed near the surface, but their distribution was not symmetric with respect to the loading axis. Glide loops nucleated at different indenter displacements (i.e., at different times), grew in-plane with little interaction. And unlike in Al, plastic deformation tends to localize in an asymmetric fashion despite the threefold symmetry of the setup. The immediate lock formation observed in Al is also absent, perhaps due to the elastic anisotropy of Cu and the inability of its widely dissociated dislocations to cross-slip. We have also observed significant twin nucleation and growth behavior.

The progression of the indentation response for both crystals can be viewed online.[40] These results show that, for a given crystal structure and indentation configuration, the critical load at which dislocation glide loops are nucleated indeed correlates with the theoretical shear strength of the material, indicating homogeneous nucleation. Further, the development of incipient plasticity subsequent to the initial load relaxation is influenced strongly by the degree of elastic isotropy, the ease of cross-slip as indicated by the intrinsic stacking fault energy, and the orientation of the loading axis with respect to the preferred slip systems of the crystal. For example, Fig. 10 illustrates the symmetry of the available slip systems for $\langle111\rangle$ and $\langle110\rangle$ indentation directions. The former configuration promotes the intersection of glide loops upon expansion, whereas the latter orientation promotes glide loop repulsion. In the next section, we explore how these elastic isotropy and orientation effects observed at the atomic scale affect the far-field indentation response.

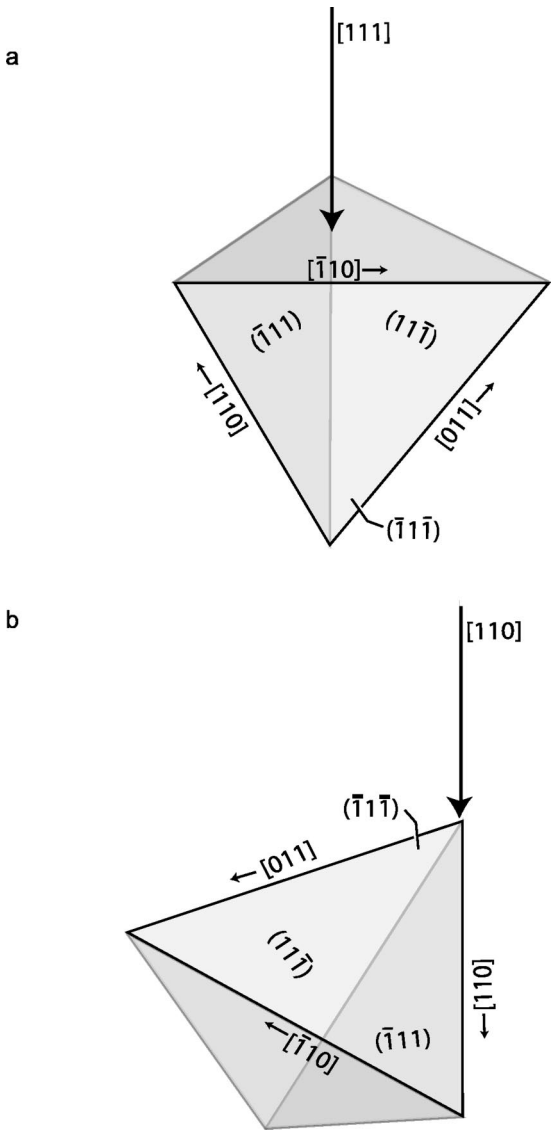

FIG. 10. Indentation direction affects the symmetry of available slip systems, either (a) promoting intersection of homogeneously nucleated glide loops on several slip planes or (b) promoting repulsion of such loops.

B. Correlation of local stress and external loading

Figure 11 illustrates the difference between the local stress developed in the crystal and the external load (far-field stress). For a dislocation to be nucleated homogeneously, the local stress in the vicinity of the nucleation site must approach the theoretical strength of the crystal, on the order of several GPa. Once a dislocation is nucleated and moves way, the local stress decreases by a certain amount. In order to nucleate homogeneously an *additional* dislocation, the local stress must climb back to the same level. However, since the previous dislocation—now supposedly piled up at the substrate—asserts a back stress on the critical region, the external loading needs to be larger than before to achieve this. Therefore we *should* observe hardening in the *P*-*h* response in a quasi-uniform sequence associated with each homogeneously nucleated dislocation, *if indeed this happens*. It is exactly the sort of hardening behavior observed in the 2D bubble raft simulations, whereby easy dislocation migration enables a sequence of homogeneous nucleation of dislocation dipoles, with an external load-displacement response of steady and quasi-uniform hardening (see Fig. 4).

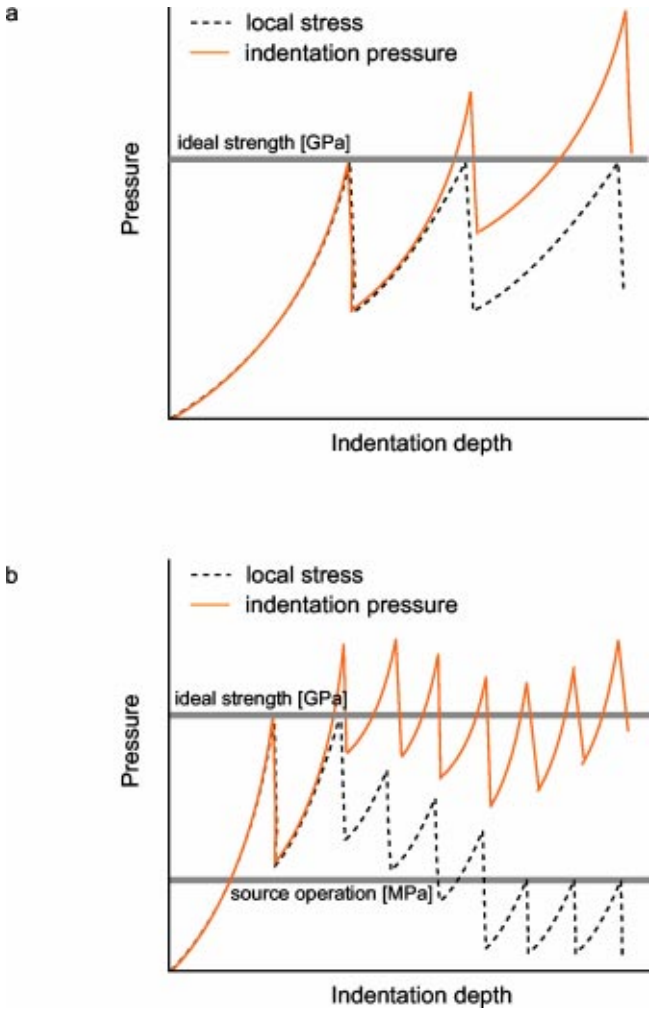

FIG. 11. (Color online) Schematic comparisons of external and internal stress evolution during incipient plasticity in crystals for two hypothetical situations. (a) All dislocations are homogeneously nucleated; (b) the first and second dislocations are homogeneously nucleated, but subsequent dislocations are heterogeneously nucleated from a source operating at a much lower stress.

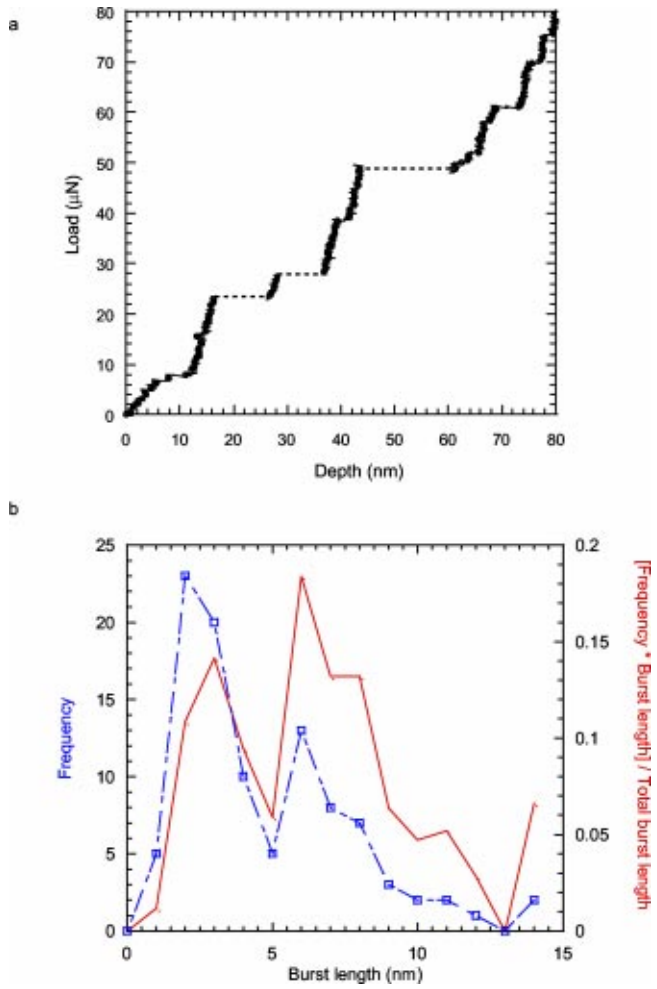

FIG. 12. (Color online) Nanoindention of {111} Al with an indenter tip radius of 150 nm. (a) Representative load-depth response, showing displacement bursts of varying length. (b) Histogram of displacement burst length (solid) and the fraction of load carried for a given burst length (dashed). Although the number frequency of short bursts is greater, the majority of stress relaxation is carried by the long bursts, corresponding to operation of defect sources.

The above indentation responses are *not* observed in actual, 3D indentation experiments. Rather, such data typically show a combination of small and large displacement relaxations, with largely varying degrees of hardening. This behavior can be rationalized by the atomic scale observations from our MD simulations. Namely, the far-field indentation load increases up to a critical value whereby dislocations are homogeneously nucleated and load relaxation is observed. Upon dislocation reaction and lock formation, indentation load again increases, indicating hardening. Then, upon increased loading, such sessile structures form sources for heterogeneous dislocation nucleation, which operate at stress levels far below the ideal strength, yielding tens of secondary dislocations that propagate to the substrate, until the local stress drops to MPa levels. In the following section, we verify this hypothesis with nominally sharp nanoindentation experiments in single-crystal Al of $\langle 111 \rangle$ orientation.

C. Experimental correlations

Bulk single-crystal {110} Al was indented in the as-received (polished) condition. Experiments were conducted on a Hysitron TriboIndenter (Hysitron Inc., Minneapolis, MN) in load control to a maximum load of approximately 100 μN, with an indenter tip radius of $\sim$150 nm. Figure 12(a) shows a representative indentation response, indicating several displacement bursts of varying lengths. All experiments showed at least three displacement bursts for this load range. The load corresponding to the first displacement burst was very consistent among experiments ($P = 10.80$ μN), corresponding to a Hertzian (linear) maximum shear stress of 2.38 GPa. This value agrees well with that calculated from MD simulations for $\langle 111 \rangle$ indentation, and with *ab initio* calculations of ideal shear strength.[38] However, as indicated in Fig. 12(b), the first displacement burst length ranged from 2 to 11 nm, with a typical length of 2–3 nm. As the Burgers

vector of Al is 0.29 nm, this burst length would correspond to almost 10 slip events and represents too large a relaxation to be explained by a single dislocation nucleation event. Thus, although the local shear stress is sufficient to induce homogeneous dislocation nucleation, the current resolution of the instrumentation may be insufficient to distinguish such a displacement burst from electronic noise.

Clearly, the distribution of displacement burst length changes with burst number. As the number of slip events increases, the burst length tends toward a bimodal distribution, centered about 1.5 nm (5 slip events) and 5 nm (17 slip events). This distribution of minor and major stress relaxations is consistent with the evolution of dislocation structure observed in the above MD simulations. Namely, dislocation interaction subsequent to an initial homogeneous nucleation event creates locks that inhibit dislocation motion and, upon continued loading, act as sources that accommodate many heterogeneously nucleated slip events for marginal increases in local stress. Back stresses from thus nucleated dislocations eventually reduce the local stress sufficiently to exhaust a particular dislocation source (minor bursts), and then further stress relaxation can be accommodated by the activation of a new source (major bursts).

As indicated in Fig. 12(b), the number of minor bursts exceeds that of major bursts in a given experiment or set of experiments. However, we can also interpret these bursts as contributions toward stress relaxation (CSR),

$$\mathrm{CSR} \equiv \frac{fl}{L}, \tag{17}$$

where f is frequency, l is the length of an individual burst and L is the sum total of all burst lengths for a given experiment or set of experiments. From this viewpoint, we show that the majority of stress relaxation is carried by major bursts, a finding consistent with our MD observations that indicate major stress relaxation events corresponding to continuous operation of defect sources.

VI. DISCUSSION

In this work we have performed a study of nucleation of single dislocations and the initial stages of dislocation loop formation in fcc metals by combining molecular dynamics and finite-element simulations with nanoindentation experiments. An energetic, atomic-scale elastic stability criterion, the Λ criterion, is shown to accurately predict the site and slip character of homogeneous dislocation emission, while the simulations capture the effects of nonlinearity, crystal anisotropy, and lattice periodicity in describing local yield processes on the microscopic scale. Correlation of the atomistic mechanisms revealed by molecular dynamics with experimentally observed load-displacement responses indicates that incipient plasticity proceeds via heterogeneous dislocation sources such as sessile locks operating locally at greatly reduced stress thresholds.

The Λ criterion, first introduced by Hill,[19] is similar to the elastic stability criterion for homogeneous deformation, considered by Wallace[41] and later refined, in that both may be derived from free energy considerations. However, these two criteria describe different conditions with respect to the internal loading. For the local instability represented by the Λ criterion, the ''weak'' point in the material is assumed to be isolated from the external boundary, so the Hemholtz free energy F is the appropriate thermodynamic potential for the process. In contrast, for the elastic instability under homogeneous deformation,[21,42,43] the Gibbs free energy is the appropriate potential because the externally applied work is in direct contact with the material volume that becomes elastically unstable. Just as Eq. (1) is the curvature of the Hemholtz free energy change, the elastic stiffness coefficient governs structural stability under homogeneous deformation at finite strain.[41]

Another general observation that deserves mention is that the application of Eq. (4) provides a quantitative measure of the weakest spot in the system, with regard to both spatial location and vibrational instability. In this respect, it would be interesting to cast the Λ criterion in the formalism of a real-space Green's function that has been applied to analyze the onset of fracture in a homogeneously strained lattice.[21,44]

Beyond the theoretical significance of the Λ criterion, our practical implementation through MD and FEM has immediate applications. First, one can imagine determining Eq. (4) using electronic structure methods rather than relying on MD with classical potentials. This approach could improve the accuracy of computational simulations in materials for which a classical potential is believed to be less reliable. Second, the viability and relative simplicity of IPFEM suggest that this approach will find many applications, wherever local constitutive relations are needed in FEM calculations.

We conclude by noting that a theme that underlies a significant portion of the present study is the competitive role of dislocation nucleation relative to dislocation migration. This issue is central to other long standing problems in deformation and plasticity. In geoscience, a well-known challenge is to understand the phenomenon of weakening of quartz in the presence of water.[45] Here, the hydrolytic effects on the emission of glissile dislocations versus the gliding of existing dislocations still remain to be resolved. Application of the large strain formalism and implementation proposed in the current study may serve to advance this and related topics in which localized deformation processes are poorly understood.

ACKNOWLEDGMENTS

This work was supported by the Defense University Research Initiative on NanoTechnology (DURINT) on ''Damage and Failure Resistant Nanostructured Materials and Interfacial Coatings,'' which is funded at MIT by the Office of Naval Research, Grant No. N00014-01-0808. We thank A.S. Argon for insightful comments. K.J.V.V. gratefully acknowledges the support of the National Defense Science and Engineering Graduate program. J.L., T.Z. and S.Y. acknowledge support by Honda R&D Co., Ltd., AFOSR (Grant No. F49620-00-10082), NSF (Grant No. DMR-9980015), and Lawrence Livermore National Laboratory under an ASCI-Level 2 grant.

*Present address: Department of Surgery, Children's Hospital, Boston, Massachusetts 02115.
†Present address: Department of Materials Science and Engineering, The Ohio State University, Columbus, Ohio 43210.
‡Electronic address: ssuresh@mit.edu

[1] J.R. Rice, R. Thomson, Philos. Mag. **29**, 73 (1974).
[2] J.R. Rice, J. Mech. Phys. Solids **40**, 239 (1992).
[3] J.R. Rice and G.E. Beltz, J. Mech. Phys. Solids **42**, 333 (1994).
[4] F. Cleri, S. Yip, D. Wolf, and S.R. Phillpot, Phys. Rev. Lett. **79**, 1309 (1997).
[5] O. Kraft, L.B. Freund, R. Phillips, and E. Arzt, Mater. Res. Bull. **27**, 30 (2002).
[6] C.L. Kelchner, S.J. Plimpton, and J.C. Hamilton, Phys. Rev. B **58**, 85 (1998).
[7] J.A. Zimmerman, C.L. Kelchner, P.A. Klein, J.C. Hamilton, and S.M. Foiles, Phys. Rev. Lett. **87**, 165507 (2001).
[8] J.D. Kiely and J.E. Houston, Phys. Rev. B **57**, 12 588 (1998).
[9] W.W. Gerberich, J.C. Nelson, E.T. Lilleoddenaa, P. Anderson, and J.T. Wyrobek, Acta Mater. **44**, 3585 (1996).
[10] W.W. Gerberich, S.K. Venkataraman, H. Huang, S.E. Harvey, and D.L. Kohlstedt, Acta Metall. Mater. **43**, 1569 (1995).
[11] E.B. Tadmor, M. Ortiz, and R. Phillips, Philos. Mag. A **73**, 1529 (1996).
[12] J. Li, K.J. Van Vliet, T. Zhu, S. Yip, and S. Suresh, Nature (London) **418**, 307 (2002).
[13] A. Gouldstone, H.J. Koh, K.Y. Zeng, A.E. Giannakopoulos, and S. Suresh, Acta Mater. **48**, 2277 (2000).
[14] D. Roundy, C.R. Krenn, M.L. Cohen, J.W. Morris, Phys. Rev. Lett. **82**, 2713 (1999).
[15] K.L. Johnson, *Contact Mechanics* (Cambridge University Press, New York, 1985).
[16] A. Gouldstone, K.J. Van Vliet, and S. Suresh, Nature (London) **14**, 656 (2001).
[17] W. Bragg and J.F. Nye, Proc. R. Soc. London, Ser. A **190**, 474 (1947).
[18] W.M. Lomer, Proc. Cambridge Philos. Soc. **45**, 660 (1949).
[19] R. Hill, J. Mech. Phys. Solids **10**, 1 (1962).
[20] J.R. Rice, in *Theoretical and Applied Mechanics*, edited by W.T. Koiter (North-Holland, New York, 1976), p. 207.
[21] J. Wang, J. Li, S. Yip, S. Phillpot, and D. Wolf, Phys. Rev. B **52**, 12 627 (1995).
[22] J. Li, J. Chang, K.J. Van Vliet, T. Zhu, S. Suresh, and S. Yip (unpublished).
[23] J. Li and S. Yip, Comput. Modeling Eng. Sci. **3**, 219 (2002).
[24] J.R. Ray, Comput. Phys. Rep. **8**, 109 (1988).
[25] T. Egami, K. Maeda, and V. Vitek, Philos. Mag. A **41**, 883 (1980).
[26] J. Li, L.J. Porter, and S. Yip, J. Nucl. Mater. **255**, 139 (1998).
[27] G. Cardano, *Ars Magna* (Milan, 1545).
[28] *ABAQUS Theory Manual*, Version 6.1 (Hibbitt, Karlsson and Sorensen, Pawtucket, RI, 2000).
[29] M. Ortiz and R. Phillips, Adv. Appl. Mech. **36**, 1 (1999).
[30] T. Zhu, J. Li, K.J. Van Vliet, R.D. Boyer, S. Suresh, and S. Yip (unpublished).
[31] R. Phillips, D. Rodney, V. Shenoy, E. Tadmor, and M. Ortiz, Modell. Simul. Mater. Sci. Eng. **7**, 769 (1999).
[32] R.D. Boyer, T. Zhu, J. Li, K.J. Van Vliet, S. Suresh, and S. Yip (unpublished).
[33] C.W. Gear, *Numerical Initial Value Problems in Ordinary Differential Equation* (Prentice-Hall, Englewood Cliffs, N.J., 1971).
[34] H.J.C. Berendsen, J.P.M. Postma, W.F. van Gunsteren, A. DiNola, and J.R. Haak, J. Chem. Phys. **81**, 3684 (1984).
[35] G.J. Ackland, D.J. Bacon, A.F. Calder, and T. Harry, Philos. Mag. A **75**, 713 (1997).
[36] C. Hwu and C.W. Fan, Int. J. Solids Struct. **35**, 3945 (1998).
[37] F. Ercolessi and J.B. Adams, Europhys. Lett. **26**, 583 (1994).
[38] C.R. Krenn, Ph.D. thesis, E.O. Lawrence Berkeley National Laboratory (2000).
[39] E. Tadmor, R. Miller, R. Phillips, and M. Ortiz, J. Mater. Res. **14**, 2233 (1999).
[40] Animated images (.avi) of MD simulations of indentation of 3D Al and Cu can be viewed at http://ninas.mit.edu/MDMovies/.
[41] D.C. Wallace, *Thermodynamics of Crystals* (Wiley, New York, 1972).
[42] Z. Zhou and B. Joos, Phys. Rev. B **54**, 3841 (1996).
[43] J.W. Morris, Jr., and C.R. Krenn, Philos. Mag. A **80**, 2827 (2000).
[44] C.S. Jayanthi, M. Tang, S.Y. Wu, J.A. Cocks, and S. Yip, Phys. Rev. Lett. **79**, 4601 (1997).
[45] A. Post and J. Tullis, Tectonophysics **295**, 117 (1998).
[46] S. Suresh, T.-G. Nieh, and B.W. Choi, Scr. Mater. **41**, 951 (1999).
[47] A.M. Minor, J.W. Morris, and E.A. Stach, Appl. Phys. Lett. **79**, 1625 (2001).
[48] Andrew Minor (personal communication).
[49] S.G. Corcoran, R.J. Colton, E.T. Lilleodden, and W.W. Gerberich, Phys. Rev. B **55**, 16 057 (1997).
[50] K.J. Van Vliet, A. Gouldstone, and S. Suresh (unpublished data).